Photoelectrocatalytic N_2 fixation and C-H oxyfunctionalization driven by H_2O oxidation

Kim, Chang Hyun; Kim, Jinhyun; Hollmann, Frank; Park, Chan Beum

DOI
10.1016/j.apcatb.2023.122925

Publication date
2023

Document Version
Final published version

Published in
Applied Catalysis B: Environmental

Applied Catalysis B: Environmental 336 (2023) 122925

Contents lists available at ScienceDirect

Applied Catalysis B: Environmental

journal homepage: www.elsevier.com/locate/apcatb

Photoelectrocatalytic N_2 fixation and C-H oxyfunctionalization driven by H_2O oxidation

Chang Hyun Kim [a,1], Jinhyun Kim [a,b,1], Frank Hollmann [c], Chan Beum Park [a,*]

[a] Department of Materials Science and Engineering, Korea Advanced Institute of Science and Technology (KAIST), 335 Science Road, Daejeon 305–701, Republic of Korea
[b] Department of Chemical and Biomolecular Engineering, University of California, Berkeley, Berkeley, CA 94720, USA
[c] Department of Biotechnology, Delft University of Technology, Van der Maasweg 9, 2629 Hz Delft, The Netherlands

ARTICLE INFO

Keywords:
Biocatalysis
Nitrogen fixation
Oxygenation
Photoelectrocatalysis
Solar fuel

ABSTRACT

Solar-driven N_2 fixation offers a green alternative to the highly energy-intensive Haber-Bosch process that releases more than 300 million metric tons of CO_2 annually to form NH_3. However, N_2-reducing photoelectrochemical (PEC) studies have not elucidated how an oxidation reaction affects the N_2 reduction reaction (NRR). Here, we report a bias-free PEC platform for N_2 reduction to NH_3 and H_2O oxidation to O_2 and H_2O_2. Under solar light, the molybdenum-doped bismuth vanadate-based photoanodes extract electrons from H_2O and transfer them to the silicon photovoltaic-wired hematite photocathode. The light-absorbing cathode receives the electrons to drive the NRR, which is influenced by the H_2O oxidation reaction's conditions. Furthermore, the integration of PEC NRR with H_2O_2-dependent biocatalytic oxyfunctionalization achieves simultaneous synthesis of valuable chemicals on both electrodes. This work presents the first example of a PEC NRR platform coupled with H_2O oxidation and H_2O_2-dependent oxygenation for unbiased chemical synthesis using N_2, H_2O, and sunlight.

1. Introduction

Ammonia (NH_3) serves as a fertilizer and an alternative carrier of hydrogen energy [1]. Currently, industrial production of NH_3 relies on the conventional Haber-Bosch process that entails the reaction between N_2 and H_2 using iron-based catalysts [1]. However, the process suffers from consuming over 1% of the global energy production because it operates at high temperature (300–500C) and pressure (200–300 atm) to dissociate the inert N≡N bond [2,3]. In addition, the reductant H_2 is produced through steam reforming of natural gas, which emits over 300 million metric tons of CO_2 per year, accounting for approximately 1.4% of global CO_2 emissions [1,3].

As an alternative to the energy-intensive and environmentally unfriend process, aqueous redox chemistry for N_2 reduction to NH_3 has garnered high interest because of (i) better energy efficiency than the Haber-Bosch process by about 20% [4], (ii) no requirement of fossil fuels (and the consequent eradication of CO_2 emission) [5], and (iii) ambient reaction conditions [6]. The N_2 reduction reaction (NRR) requires electrons that are provided by external power source (e.g., potentiostat) [1,3] or sacrificial electron donor (e.g., methanol [7] or ascorbate [8]). For example, recently reported N_2-reductive photoelectrochemical (PEC) systems [9,10] use electrical energy [e.g., −0.1 to −0.2 V vs. the reversible hydrogen electrode (RHE)] in a three-electrode configuration. We envision that the need for electrical energy and artificial electron donors can be eliminated by solar-driven extraction of electrons from H_2O, which functions as an abundant electron donor and a biocompatible solvent [11–13].

Here, we report the first example of unbiased N_2 reduction to NH_3 fueled by H_2O ($2N_2 + 6H_2O$ + sunlight → $4NH_3 + 3O_2$) in a two-electrode configuration. As illustrated in Fig. 1, the N_2-reductive PEC system consists of two components: (i) a ferric oxyhydroxide-coated, molybdenum-doped bismuth vanadate ($FeOOH/Mo:BiVO_4$) photoanode that extracts electrons from H_2O and (ii) a Si photovoltaic (Si PV)-wired hematite ($Si/\alpha\text{-}Fe_2O_3$) photocathode that supplies a large photovoltage (V_{ph}) for bias-free redox reactions, receives the electrons from the photoanode, and achieves the six-electron reduction of N_2 to NH_3 at the surface of $\alpha\text{-}Fe_2O_3$ nanorods. Furthermore, we designed a bias-free combination of NRR with H_2O_2 production driven by two-electron

* Corresponding author.
E-mail address: parkcb@kaist.ac.kr (C.B. Park).
[1] These authors contributed equally to this work.

https://doi.org/10.1016/j.apcatb.2023.122925
Received 5 March 2023; Received in revised form 25 May 2023; Accepted 28 May 2023
Available online 2 June 2023

WOR ($N_2 + 6H_2O$ + sunlight → $2NH_3 + 3H_2O_2$) (Fig. 1). The in situ generated H_2O_2 activates H_2O_2-dependent peroxygenases for enantioselective oxyfunctionalization of inert C-H bonds. This peroxygenase-catalyzed hydroxylation converts simple organic compounds into value-added building blocks used in the synthesis of fine chemicals and pharmaceutical intermediates [14,15].

2. Experimental section

2.1. Materials

Iron nitrate nonahydrate, sodium sulfate, ammonium chloride, ammonium-^{15}N chloride, salicylic acid, sodium citrate tribasic dihydrate, sodium hypochlorite, sodium nitroferricyanide, hydrazine hydrate, 4-(dimethylamino)benzaldehyde, sodium chloride, potassium chloride, bismuth nitrate pentahydrate, potassium iodide, vanadyl acetylacetonate, dimethyl sulfoxide, *p*-benzoquinone, bis(acetylacetonato) dioxomolybdenum, iron sulfate heptahydrate, horseradish peroxidase, and 2,2′-azino-bis(3-ethylbenzothiazoline-6-sulfonic acid) were purchased from Sigma Aldrich (St. Louis, MO, USA). All chemicals were used without further purification. We used type 1 ultrapure water (18 MΩ cm) from a Direct-Q® 5 UV ultrapure water purification system (Millipore Corp., USA). We prepared a recombinant, evolved peroxygenase from *Agrocybe aegerita* (r*Aae*UPO) according to the literature [12].

2.2. Synthesis of photocathodes

We slightly modified a reported synthetic method [16] to prepare a hematite electrode via hydrothermal method and high-temperature annealing. A commercial carbon cloth was purchased and washed with acetone, ethanol, and deionized water. For deposition of a β-FeOOH film on the carbon cloth, we first prepared an aqueous solution containing 0.06 M $Fe(NO_3)_3{\cdot}9H_2O$ and 0.06 M Na_2SO_4. Then, we sealed the carbon cloth and the clear solution in a Teflon-lined stainless steel autoclave, which was heated in a furnace (Fisher Scientific Co., USA) at 120 °C for 6 h. To transform β-FeOOH into α-Fe_2O_3, we annealed the β-FeOOH electrode under N_2 flow at 400 °C for 4 h with a heating rate of 1.5 °C min^{-1}. To prepare a Si/α-Fe_2O_3 photocathode, we wired the as-synthesized α-Fe_2O_3 cathode to a commercial Si photovoltaic (Si PV). The electron-collecting contact area of the Si PV was wired to the α-Fe_2O_3 electrode. The Si PV's hole-collecting contact area was wired to the F:SnO_2 (FTO) side of the photoanode using Cu tape.

2.3. Photoelectrochemical N_2 reduction and ammonia quantification

We performed PEC NRR in a three-electrode configuration consisting of a working electrode, a reference electrode (Ag/AgCl, 3 M NaCl), and a counter electrode (carbon cloth). We purged 0.1 M Na_2SO_4 electrolyte with the high-purity N_2 gas (purity: 99.999%) before and during PEC reactions. All potentials were quoted versus the reversible hydrogen electrode (RHE) according to Eq. 1:

$$E_{RHE}\ (V) = E_{Ag/AgCl}\ (V) + 0.209 + 0.059 \times pH \quad (1)$$

We quantified ammonia using the indophenol blue method with some modifications [1]. We collected 1 mL of a reaction solution, which was mixed with NaOH solution (1 mL, 1 M) containing salicylic acid (5 wt%) and sodium citrate (5 wt%), NaClO solution (0.5 mL, 0.05 M), and sodium nitroferricyanide solution (0.1 mL, 1 wt%). After stirring for 2 h in dark, we used an ultraviolet-visible (UV-Vis) spectrophotometer (JASCO Inc., Japan) to obtain the absorption spectrum of the mixture solution at 655 nm. The NH_3 production rate and Faradaic efficiency were calculated using Eqs. 2 and 3:

$$\text{Production rate}(\mu g\ h^{-1}\ cm^{-2}) = \frac{c_{NH3} \times V}{t \times A} \quad (2)$$

$$\text{Faradaic efficiency}(\%) = \frac{3 \times F \times c_{NH3} \times V}{17 \times Q} \times 100 \quad (3)$$

where c_{NH3} is the NH_3 concentration (μg mL^{-1}), V is the volume of the electrolyte (mL), t is the reaction time (h), A is the geometrical surface area of the electrode (cm^2), F is the Faraday constant (96,485 C mol^{-1}), and Q is the total charge consumed during photoelectrocatalysis. The solar-to-ammonia (STA) conversion efficiency was estimated in a two-electrode configuration according to the Eq. 4:

$$STA\ (\%) = \frac{r \times \Delta G}{I \times A} \times 100 \quad (4)$$

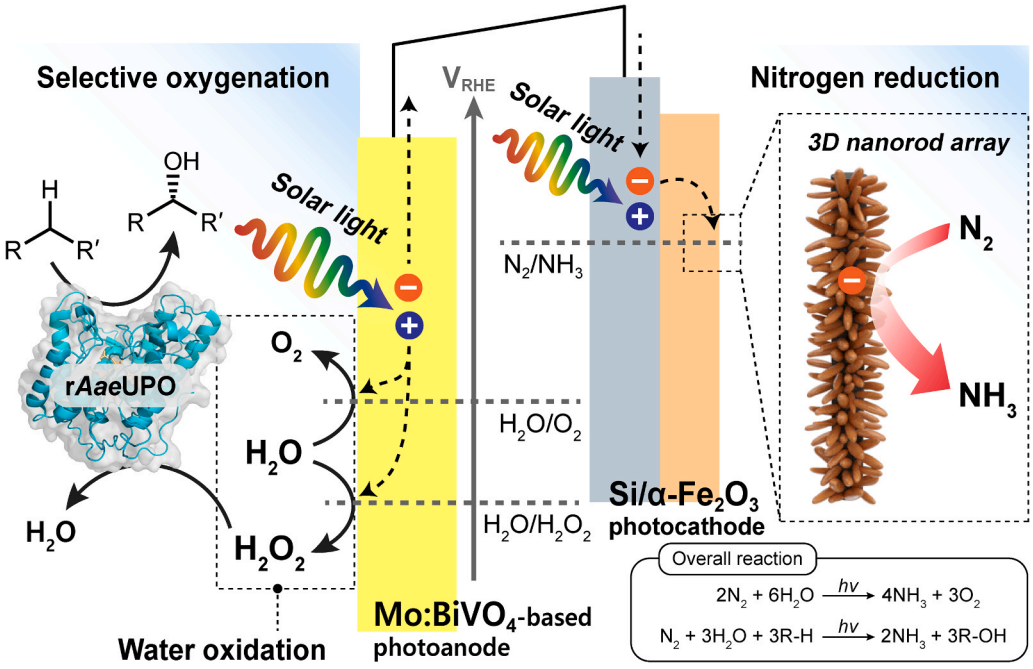

Fig. 1. Schematic illustration of unbiased paring of N_2 reduction with H_2O oxidation and enantioselective enzymatic synthesis. A Si-wired hematite (Si/α-Fe_2O_3) photocathode reduces N_2 to NH_3 while a water-oxidizing Mo:$BiVO_4$-based photoanode extracts electrons from H_2O as an electron donor. The Si/α-Fe_2O_3 is electrically connected with a Mo:$BiVO_4$ for producing NH_3 and H_2O_2 at cathodic and anodic sites, respectively. The in situ generated H_2O_2 activates r*Aae*UPO for enantioselective oxyfunctionalization reactions.

where r is the NH_3 production rate (mmol s^{-1}), ΔG is the Gibbs free energy of overall NRR (330 kJ mol^{-1}), and I is the light density (100 mW cm^{-2}). For H_2 quantification, we used a micro gas chromatograph (Micro GC fusion, INFICON Inc., USA) that was equipped with a micro thermal conductivity detector and a Molsieve 5 A column.

2.4. Hydrazine quantification

We quantified N_2H_4 using Watt and Chrisp method [1]. We prepared a coloring solution by dissolving 0.6 g of *p*-$C_9H_{11}NO$ in a mixture solution of 30 mL absolute ethanol and 3 mL concentrated HCl. Typically, 0.5 mL of a reaction solution was mixed with 0.5 mL of the coloring solution. After stirring for 10 min in dark, the UV-Vis spectra of the mixture solution were acquired at 455 nm.

2.5. Nuclear magnetic resonance spectroscopic analysis

We recorded ^1H nuclear magnetic resonance (^1H NMR) spectra using a Bruker AVANCE NEO 500 MHz to detect NH_3. After PEC reduction of $^{14}N_2$, a reaction solution was collected and acidified with 0.5 M H_2SO_4. Subsequently, we mixed the acidified reaction solution with [D_6]dimethylsulfoxide ([D_6]DMSO) and a maleic acid as a solvent and an internal standard, respectively. We used zgesfpgp as the NMR pulse sequence with 128 and 2048 scans for qualitative and quantitative analyses, respectively. When we isotope labeling experiment, we used $^{15}N_2$ gas (Sigma-Aldrich, 98 atom % ^{15}N) as a feeding gas and set the NMR scan number to 1024.

2.6. Preparation of photoanodes

We rinsed a commercial FTO glass with KOH solution, deionized water, and ethanol. We prepared a precursor solution by dissolving Bi$(NO_3)_3{\cdot}5H_2O$ (0.04 M), HNO_3 (2 μL mL^{-1}), and KI (0.4 M) in deionized water (25 mL) and then adding 10 mL of absolute ethanol containing *p*-benzoquinone (0.23 M). The FTO substrate was immersed in the precursor solution, and the cathodic bias of −0.1 V (vs. Ag/AgCl) was applied for 3 min using a potentiostat/galvanostat (WMPG 1000, WonATech Co., Korea). For transformation of BiOI into Mo:$BiVO_4$, we uniformly dropped a DMSO solution—containing $VO(acac)_2$ (0.2 M) and $MoO_2(acac)_2$ (2 mM)—on the BiOI electrode and heated in a Lindberg/Blue M muffle furnace (Fisher Scientific Corp., USA) at 450 °C for 2 h with a heating rate of 1 °C min^{-1}. After the thermal treatment, we immersed the sample in a 1 M NaOH solution with gentle stirring to eliminate unwanted V_2O_5 crusts. For photo-assisted electrodeposition of FeOOH adlayer on the Mo:$BiVO_4$ electrode, we dissolved 0.1 M $FeSO_4{\cdot}7H_2O$ in N_2-enriched deionized water and immersed the Mo:$BiVO_4$ in the solution. Then, we applied 0.25 V (vs. Ag/AgCl) to a Mo:$BiVO_4$ electrode under irradiation (2 mW cm^{-2}) for 20 min.

2.7. Photoelectrochemical analysis of photoanodes

We adopted a three-electrode configuration consisting of Ag/AgCl (3 M NaCl) as a reference electrode and Pt wire as a counter electrode. We used phosphate-buffered saline (PBS) (10 mM, pH 7.0) as an anolyte solution. We conducted linear sweep voltammetric and chronoamperometric analyses using a potentiostat/galvanostat (WMPG 1000, WonATech Co., Korea). We used an impedance analyzer (ZIVE SP1, WonATech Co., Korea) to acquire Nyquist plots at a frequency of 100 kHz to 0.1 Hz and an AC potential amplitude of 25 mV. We used a xenon lamp as a light source.

2.8. Material characterization

The morphologies of electrodes were investigated using an SU8230 field emission scanning microscope (SEM; Hitachi Co., Japan) and a transmission electron microscope (TEM; Talos F200X, FEI Company, USA). X-ray photoelectron spectroscopy (XPS; Thermo VG Scientific, UK) was used to confirm the elemental components of electrodes. The crystal structures of electrodes were examined using X-ray diffractometer (XRD; RIGAKU Co. Japan) with a Cu Kα radiation wavelength of 1.5418 Å. UV-Vis absorption and transmittance spectra of photoelectrodes were obtained using UV-Vis spectrophotometer (Perkin Elmer, USA). Photoluminescence spectra were recorded by a spectrofluorometer (RF-6000, SHIMADZU Co., Inc., Japan).

2.9. H_2O_2 quantification

We used 2,2′-azino-bis(3-ethylbenzothiazoline-6-sulfonic acid) (ABTS) assay to quantify H_2O_2. After driving Mo:$BiVO_4$-driven photoanodic reactions, we collected a reaction solution and mixed it with a colorimetric reagent [potassium phosphate solution (100 mM, pH 5.0) containing 2.5 U horseradish peroxidase and 2 mM ABTS]. After incubated at room temperature for 10 min, the absorbance of the mixture was monitored using the UV-Vis spectrophotometer at 420 nm.

2.10. Bias-free photoelectrocatalytic N_2 reduction coupled with H_2O oxidation and biocatalytic oxyfunctionalization reactions

We coupled NRR with H_2O oxidation reaction in a two-compartment configuration, which was connected by a salt bridge. The light source was a 450 W xenon-arc lamp (Newport Co., USA). We immersed a α-Fe_2O_3 cathode in 0.1 M Na_2SO_4 electrolyte (pH 7.0) and a FeOOH/Mo:$BiVO_4$ photoanode in a PBS solution (10 mM, pH 7.0). The Si PV was placed in front of a cathodic cell, and connected to the α-Fe_2O_3 cathode. The geometrical surface areas of FeOOH/Mo:$BiVO_4$, α-Fe_2O_3, and Si PV were 1, 1, and 6 cm^2, respectively. For coupling of PEC NRR with photobiocatalytic reaction, we substituted FeOOH/Mo:$BiVO_4$ with Mo:$BiVO_4$. We prepared an anodic chamber with the PBS solution (10 mM, pH 7) containing 20 nM r*Aae*UPO and a substrate. After the photoenzymatic reactions, we quantified enzymatic products by a 7890 A gas chromatograph (Agilent Technologies Inc., USA) equipped with a CP-Chirasil-Dex CB column (25 m, 0.32 mm, 0.25 μm) [12]. We extracted an enzymatic product from a reaction sample using ethyl acetate (containing 5 mM 1-octanol as the internal standard), and dried it over $MgSO_4$. The detailed oven-temperature programs were tabulated in Table S1. The enantiomeric excess (e.e.), total turnover number (TTN), and turnover frequency (TOF) of r*Aae*UPO were calculated according to the Eqs. 3, 4, and 5 as follows:

$$\text{e.e.}(\%) = \frac{|\text{Mole of an enantiomer} - \text{Mole of the other enantiomer}|}{\text{Total moles of products}} \times 100 \quad (3)$$

$$\text{TTN}_{\text{rAaeUPO}} = \frac{\text{Maximum concentration of product}}{\text{Concentration of r}Aae\text{UPO}} \quad (4)$$

$$\text{TOF}_{\text{rAaeUPO}}(h^{-1}) = \frac{\text{Turnover number of r}Aae\text{UPO}}{\text{Time}} \quad (5)$$

3. Results

3.1. Si/α-Fe_2O_3 photocathode for N_2 fixation

We synthesized a Si/α-Fe_2O_3 photocathode by (i) the formation of β-FeOOH layer on a carbon cloth, (ii) the thermal phase transformation from β-FeOOH to α-Fe_2O_3 under N_2-rich conditions (purity: 99.999 %), and (iii) electrical wiring α-Fe_2O_3 with a Si PV in a series. As shown in the plan-view scanning electron microscopic image (Fig. 2a), the as-synthesized α-Fe_2O_3 exhibited a three-dimensional nanostructure consisting of nanorods (diameter: ~50 nm). We verified that the nanostructured ferric oxide exhibited the α-Fe_2O_3 phase using X-ray diffraction analysis (Fig. 2b). Next, we performed X-ray photoelectron spectroscopy (XPS) on the α-Fe_2O_3 electrocatalyst, and verified that it

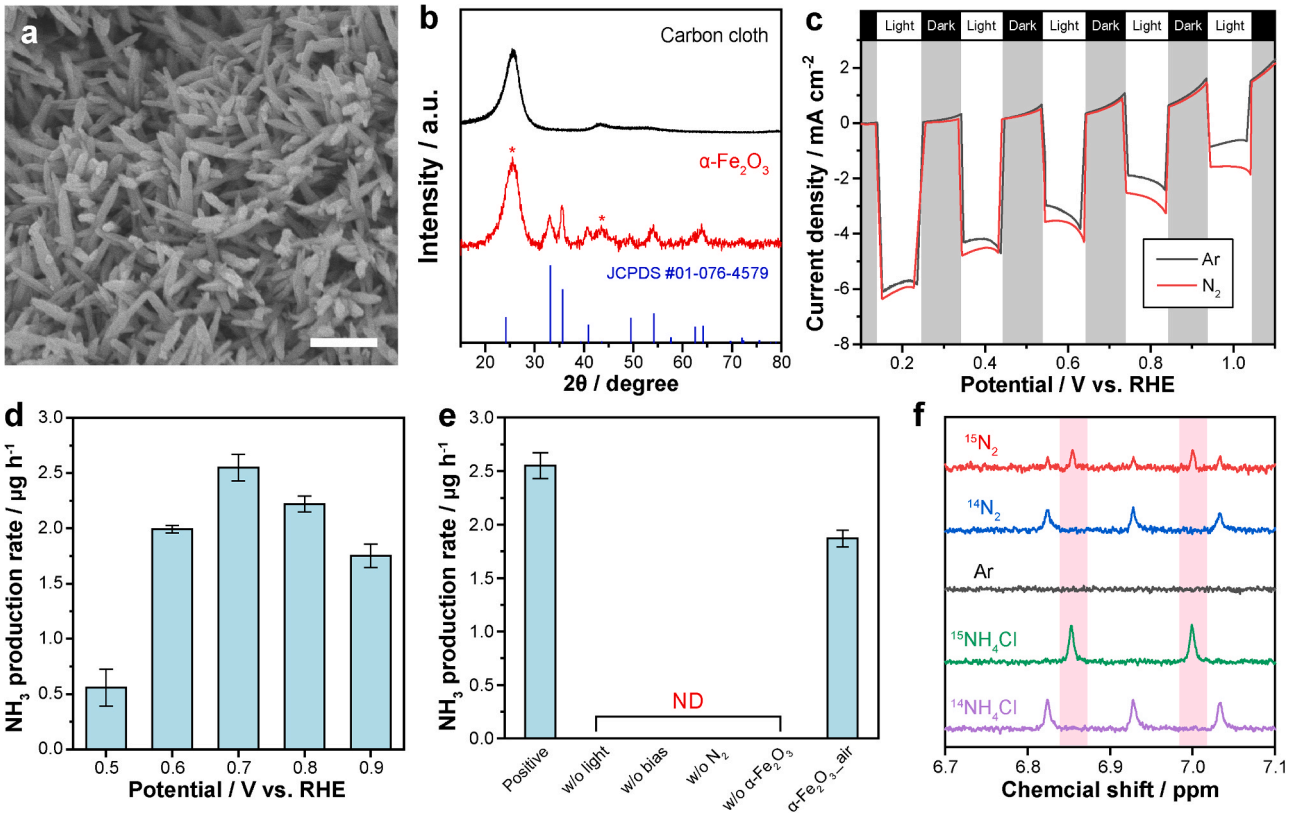

Fig. 2. Photoelectrochemical N_2-to-NH_3 conversion using Si/α-Fe_2O_3 photocathode. (a) Plan-view SEM image of α-Fe_2O_3. Scale bar: 500 nm. (b) XRD patterns of carbon cloth and α-Fe_2O_3. The diffraction file number of α-Fe_2O_3 is #01–076–4579, which is provided by the joint committee on powder diffraction standards-international center for diffraction data. Asterisks denote the XRD peaks of carbon cloth. (c) Chopped linear sweep voltammograms of Si/α-Fe_2O_3 under Ar- or N_2-enriched environments. Scan rate: 20 mV s^{-1}. Electrolyte: 0.1 M Na_2SO_4 aqueous solution. (d) NH_3 production rates of the Si/α-Fe_2O_3 photocathode at different applied potentials. (e) A series of control experiments for PEC NRR by Si/α-Fe_2O_3. Potential: 0.7 V (vs. RHE). (f) ^{1}H NMR spectra of PEC NRR experiments. Feed gas: $^{15}N_2$ or $^{14}N_2$. Geometrical surface area of the photocathode in (c-f): 1 cm^2. Reaction time in (d-f): 2 h. Light intensity in (c-f): 1 sun (air mass 1.5 global, 100 mW cm^{-2}). Electrolyte volume in (c-f): 30 mL. Error bars correspond to the standard deviation ($n = 3$). ND: not detected.

contained Fe and O atoms in the Fe^{3+} and O^{2-} states, respectively (Fig. S1). Under 1-sun irradiation (air mass 1.5 global, 100 mW cm^{-2}), the $J-V$ plot of Si/α-Fe_2O_3 was anodically shifted by 1.25 V than that of α-Fe_2O_3 (Fig. S2), which we attribute to the Si PV's V_{ph}. It indicates that Si/α-Fe_2O_3 photocathode requires a less cathodic bias than α-Fe_2O_3 cathode under solar light.

We demonstrated the capability of Si/α-Fe_2O_3 photocathode to convert N_2 into NH_3 in a three-electrode configuration under 1-sun illumination. According to our chopped linear sweep voltammograms (Fig. 2c), the Si/α-Fe_2O_3 produced an anodic current density in N_2-enriched 0.1 M Na_2SO_4 solution under dark conditions, indicating imperceptible NRR reactions. In stark contrast, the photocathode generated much higher photocathodic current density under N_2-rich conditions than Ar-rich conditions (Fig. 2c), signifying the transfer of photoexcited electrons to N_2 molecules. Controlled potential photoelectrolysis (CPPE) demonstrated NH_3 production from 0.5 to 0.9 V (vs. the reversible hydrogen electrode, RHE) (Fig. 2d). We quantified NH_3 using the indophenol blue method and UV-Vis spectroscopy because UV-Vis and quantitative ^{1}H nuclear magnetic resonance (NMR) tools provide no significantly different concentrations of NH_3 in statistics (see Fig. S3 for details). The highest average NH_3 production rate and Faradaic efficiency were 2.55 μg h^{-1} at 0.7 V (vs. RHE) and 10.3% at 0.8 V (vs. RHE), respectively (Figs. 2d and S4). The application of more negative potentials than 0.7 V (vs. RHE) decreased NH_3 production rates. We attribute the result to the competing hydrogen evolution reaction (HER) (Fig. S5) from the proton adsorption on the α-Fe_2O_3 surface [17,18]. Control experiments in the absence of light, electrical bias, N_2, or α-Fe_2O_3 did not produce NH_3 (Fig. 2e), and N_2 feed gas itself did not contain NH_3 (Fig. S6a). In addition, hydrazine (N_2H_4) was not formed as a side product at 0.7 V (vs. RHE) (Figs. S7 and S8), which highlights the Si/α-Fe_2O_3's excellent selectivity toward NRR. Furthermore, we confirmed the robust stability of Si/α-Fe_2O_3-driven NRR. As shown in Fig. S9, Si/α-Fe_2O_3 exhibited (i) steady NH_3 production rates along with photocathodic currents and (ii) no change in morphology and crystallographic structure during a five-iteration experiment.

We performed isotope labeling experiments to identify the chemical source of NH_3. According to our ^{1}H NMR spectroscopy, Si/α-Fe_2O_3 formed $^{14}NH_4^+$ in a $^{14}N_2$-enriched solution after CPPE (1 sun, 0.7 V vs. RHE, 2 h) (Fig. 2f), and $^{14}N_2$ feed gas did not contain $^{14}NH_3$ (Fig. S6b). The substitution of $^{14}N_2$ with $^{15}N_2$ resulted in the generation of $^{15}NH_4^+$ (Fig. 2f), which indicates that NH_3 production originated from the PEC NRR, not NO_3^- reduction or NH_3 pollution. We also detected ^{14}N triplet NMR peaks in the isotope experiment, which we attribute to the dissolution of atmospheric $^{14}N_2$ into the $^{15}N_2$-containing electrolyte solution. The control experiment using Ar gas did not show NH_4^+'s NMR peaks (Fig. 2f), reaffirming the Si/α-Fe_2O_3-driven NRR to NH_3.

The oxygen vacancy (O_V) of a metal oxide (e.g., WO_3 [19], TiO_2 [20,21], $LaFeO_3$ [22]) has been reported to function as an active site that accelerates catalytic reactions by, for example, absorbing N_2 molecules, facilitating hydrogenation steps, and/or decreasing the free energy change at a potential-determining step (Table S2). Thus, we investigated the effect of α-Fe_2O_3's O_V in N_2 fixation to NH_3. We synthesized α-Fe_2O_3 that was annealed in air (namely, α-Fe_2O_3_air) during thermal phase transformation. According to our O 1s XPS analysis (Fig. S10), the substitution of N_2 with air resulted in a lower abundance of O_V by 7%p, which we attribute to the role of O_2 molecules [23] to suppress the

formation of O_V during thermal treatment of metal oxides. We found that NH_3 production rate of the Si/α-Fe_2O_3 was 1.37 times higher than that of the Si/α-Fe_2O_3_air photocathode. We speculate that an increase in the concentration of α-Fe_2O_3's O_V may boost N_2 adsorption and/or N≡N activation based on literature on density functional theory calculations that elucidate the important role of metal oxides' O_V in accelerating NRR.

3.2. FeOOH/Mo:$BiVO_4$ photoanode for H_2O oxidation

To extract electrons from H_2O and supply them to the Si/α-Fe_2O_3 photocathode, we used Mo:$BiVO_4$ because of its high stability under aqueous environments and excellent WOR kinetics [24,25]. We synthesized a Mo:$BiVO_4$ electrode through (i) electrodepositing bismuth oxyiodide (BiOI) film on a fluorine-doped tin oxide and (ii) converting BiOI to Mo:$BiVO_4$ via thermal and chemical treatments. We further photoelectrochemically deposited FeOOH cocatalyst on the Mo:$BiVO_4$ photoanode because the adlayer is a highly active catalyst for H_2O oxidation at moderate potentials by suppressing surface charge recombination and minimizing the kinetic barrier [25–28]. We confirmed the formation of amorphous FeOOH layer (thickness: ~5 nm) on the crystalline Mo:$BiVO_4$ using XPS, TEM, and energy-dispersive X-ray spectroscopic elemental mapping (Figs. S11a, S11b, S11c, and S12). The FeOOH deposition did not change the Mo:$BiVO_4$'s nanostructured morphology (Fig. S11d), monoclinic scheelite phase (Fig. S11e), light absorption property, and direct bandgap (2.5 eV) (Fig. S11f).

We verified the capability of FeOOH cocatalyst to accelerate Mo:$BiVO_4$'s WOR. As shown in Fig. 3a and S13a, FeOOH/Mo:$BiVO_4$ exhibited a cathodic shift of the onset potential for H_2O oxidation (~230 mV), an enhanced photoanodic current from 0.4 to 1.4 V (vs. RHE), and a lower Tafel slope in a phosphate-buffered saline (10 mM, pH 7.0) solution. We attribute the improved WOR performance to (i) a decreased charge-transfer resistance (Figs. S13b and S13c), (ii) increased efficiency of charge transfer at the electrode|electrolyte interface (Fig. S13d), (iii) reduced charge recombination behavior (Figs. S14a and S14b), and (iv) longer decay time of charge carriers (Figs. S14c and S14d), which we obtained using electrochemical impedance spectroscopy [29], (transient) voltammetric analysis, and photoluminescence spectroscopy [30]. Detailed analytical explanations are shown in the caption of Figs. S13 and S14.

3.3. Solar-driven unbiased N_2 reduction coupled with H_2O oxidation

Having substantiated the NRR and WOR driven by Si/α-Fe_2O_3 and FeOOH/Mo:$BiVO_4$, respectively, we constructed a full PEC structure (i.e., FeOOH/Mo:$BiVO_4$|Si/α-Fe_2O_3) to drive NRR fueled by H_2O as an electron donor. We expected bias-free coupling of NRR and WOR according to the intersection of the overlaying $|J|-V$ plots of FeOOH/Mo:$BiVO_4$ and Si/α-Fe_2O_3 (Fig. 3a). The exposure of the PEC system to solar light triggered NH_3 production with an average rate of 1.476 μg h^{-1} (Fig. 3b) and a solar-to-ammonia conversion efficiency of 0.0080%. In the absence of light, Si PV, or N_2 molecules, NH_3 formation was imperceptible (Fig. 3b), which highlights the unbiased NRR to NH_3. When we substituted α-Fe_2O_3 with α-Fe_2O_3_air, the NH_3 formation rate decreased by 1.36 times. In addition, the omission of FeOOH on Mo:$BiVO_4$ decreased the production rate significantly from 1.476 to 0.328 μg h^{-1} (Fig. 3b), indicating that WOR is responsible for supplying electrons for NRR.

Based on the importance of WOR in NRR, we investigated the role of H_2O as an electron donor for unbiased NRR by FeOOH/Mo:$BiVO_4$|Si/α-Fe_2O_3 system. To control H_2O concentration in a cathodic electrolyte solution, we used an anhydrous dimethyl sulfoxide (DMSO) that is miscible with the aqueous electrolyte. Our chronoamperometric analysis shows that current density increased with increasing volume ratio of H_2O/DMSO under 1-sun illumination, and the current density was negligible under dark conditions (Figs. 3c and S15). In accordance with the result, we obtained a saturation curve that shows the relationship between the rate of NH_3 production and the H_2O/DMSO volume ratio

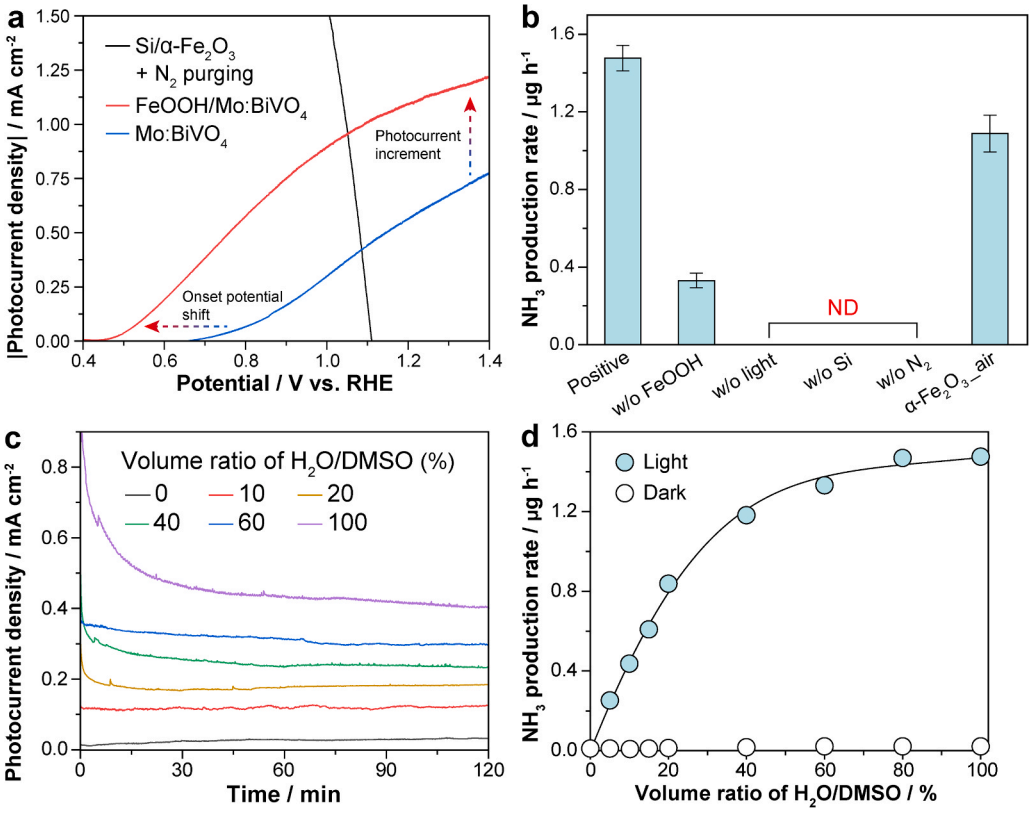

Fig. 3. Unbiased reduction of N_2 to NH_3 by the FeOOH/Mo:$BiVO_4$|Si/α-Fe_2O_3 photoelectrocatalytic system. (a) Overlap of $|J|-V$ profiles of a Si/α-Fe_2O_3 photocathode (black) and Mo:$BiVO_4$-based photoanodes (red and blue). (b) Control experiments for bias-free PEC NRR driven by FeOOH/Mo:$BiVO_4$|Si/α-Fe_2O_3. (c) Chronoamperometric curves with various H_2O/DMSO volume ratios in an anodic compartment. (d) Effect of H_2O/DMSO volume ratios on the rate of NH_3 formation. Light condition in (a-d): 1 sun. Geometrical surface areas of photocathodes and photoanodes in (a-d): 1 cm^2. Reaction time in (b, d): 2 h. Electrolyte volume in the cathodic compartment: 15 mL. Electrolyte volume in the anodic compartment: 10 mL. Error bars correspond to the standard deviation ($n = 3$). ND: not detected.

(Fig. 3d). We observed that unbiased NH_3 formation kinetics decreased with decreasing volume ratio of H_2O/DMSO, and became imperceptible when the electrolyte solution consisted of DMSO only. The result highlights the transfer of photoexcited electrons from H_2O electron donor to N_2 reactant. In addition, the NH_3 production kinetics linearly increased up to 57% of its maximal production rate until the volume ratio of H_2O/DMSO reached 20%. We ascribe it to the saturation of FeOOH/Mo:$BiVO_4$'s active sites for WOR.

Furthermore, we explored the effect of photoexcited electrons and holes on the NRR. We added sodium sulfite (Na_2SO_3) and sodium persulfate ($Na_2S_2O_8$) as a hole and electron scavenger, respectively. As shown in Fig. S16a, the addition of Na_2SO_3 to an anolyte decreased the NH_3 production rate. Although Na_2SO_3 increased the operating current of FeOOH/Mo:$BiVO_4$|Si/α-Fe_2O_3 (Fig. S16b), it shifted Si/α-Fe_2O_3's potential anodically in FeOOH/Mo:$BiVO_4$|Si/α-Fe_2O_3 architecture (Fig. S16c), and consequently decreased NH_3 production on Si/α-Fe_2O_3 (Fig. 2d). In contrast, supplementing $Na_2S_2O_8$ to a catholyte resulted in no production of NH_3 (Fig. S16a). It highlights that Si/α-Fe_2O_3's photoexcited electrons participate in NRR. Consistent with this result, Si/α-Fe_2O_3 did not generate NH_3 when we added Na_2SO_3 and $Na_2S_2O_8$ into the anolyte and catholyte, respectively, at the same time (Fig. S16a).

3.4. Photobiocatalytic oxyfunctionalization coupled with N_2 reduction

Oxidoreductases catalyze various synthetically useful reactions with exceptional selectivity and environmental benignity [31–40], which solid-state catalytic electrodes cannot achieve. In this study, we attempted to pair NRR with oxidoreductase-driven oxygenation of inert C-H bonds (Fig. 1). As a model biocatalyst, we employed the recombinant, evolved unspecific peroxygenase from *Agrocybe aegerita* (r*Aae*UPO) [12,13,41–43]. Considering that r*Aae*UPO requires H_2O_2 as a sole oxidant [41,44,45], we did not deposit FeOOH adlayer on the Mo:$BiVO_4$ photoanode. This is because FeOOH's Fermi level is more negative [46] than the redox potential [12] of two-electron WOR ($2H_2O + 2h^+ \rightarrow H_2O_2 + 2H^+$) (Fig. S17a). We confirmed that photoelectroactivated Mo:$BiVO_4$ gradually formed H_2O_2, whereas FeOOH/Mo:$BiVO_4$ formed a negligible amount of H_2O_2 (Fig. S17b).

Although Mo:$BiVO_4$ generates more H_2O_2 than FeOOH/Mo:$BiVO_4$, the target redox reaction [N_2 (g) + $6H_2O$ (l) → $2NH_3$ (aq) + $3H_2O_2$ (aq)] is rather sluggish in the Mo:$BiVO_4$|Si/α-Fe_2O_3 system. We ascribe this to Mo:$BiVO_4$'s slow electron extraction from H_2O, which results in a lower photocurrent density (Fig. 3a). To accelerate the redox reaction, we applied external electrical bias and found that ~0.5 V bias is required to optimize NH_3 production rate (Fig. S18). Based on this result, we replaced the original Si PV (V_{ph} = 1.25 V) with another Si PV having a higher V_{ph} of 1.80 V to realize bias-free coupling of NH_3 and H_2O_2 production. The theoretical and actual operation currents of Mo:$BiVO_4$|Si(1.80 V)/α-Fe_2O_3 were approximately 2.3 times higher than those of Mo:$BiVO_4$|Si(1.25 V)/α-Fe_2O_3 (Fig. S19).

Building on the results, we explored unbiased pairing of NH_3 production with enantioselective oxyfunctionalization using Mo:$BiVO_4$|Si (1.80 V)/α-Fe_2O_3 (Fig. 1). We analyzed the product using gas chromatography-mass spectrometry (GC-MS) and GC (Figs. S20a and S21a). As shown in Fig. 4a, ethylbenzene was hydroxylated to enantiopure (*R*)-1-phenylethanol [> 99% enantiomeric excess (e.e.)] with a

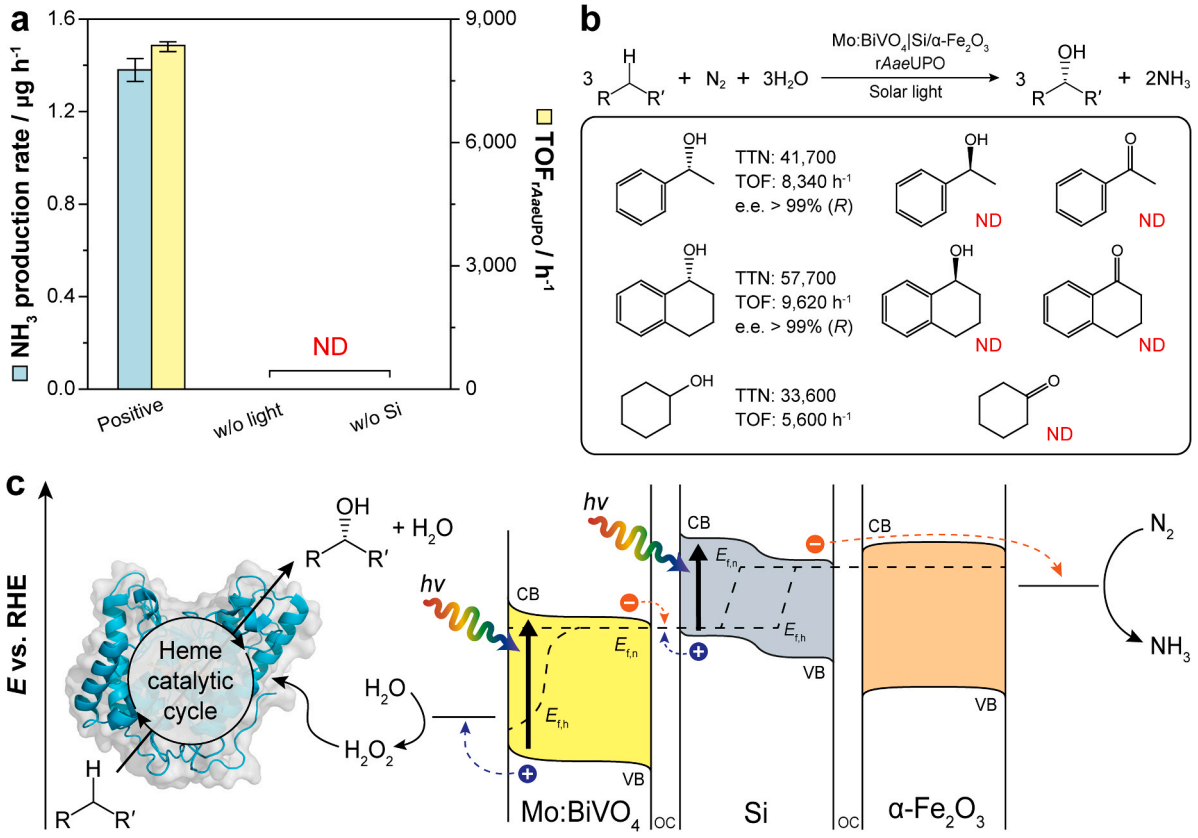

Fig. 4. Enantioselective photobiocatalytic oxyfunctionalization coupled with N_2 reduction. (a) Control experiments of bias-free biocatalytic hydroxylation paired with N_2 reduction. (b) Other r*Aae*UPO-driven oxygenation reactions driven by Mo:$BiVO_4$|Si/α-Fe_2O_3. (c) Plausible mechanism of unbiased combination of N_2 reduction and UPO biocatalysis. OC: ohmic contact. CB: conduction band. VB: valence band. $E_{f,n}$: quasi-Fermi level of electrons. $E_{f,h}$: quasi-Fermi level of holes. Catholyte in (a, b): Na_2SO_4 solution (0.1 M, 15 mL). Anolyte in (a, b): phosphate-buffered saline (10 mM, pH 7.0, 10 mL) containing r*Aae*UPO and substrate. Geometrical surface areas of photocathodes and photoanodes in (a, b): 1 cm^2. Reaction time in (b): 6 h. Light intensity in (a, b): 1 sun. Error bars correspond to the standard deviation (n = 3). ND: not detected.

turnover frequency for r*Aae*UPO ($TOF_{rAaeUPO}$) of 8340 h^{-1} and a total turnover number of r*Aae*UPO ($TTN_{rAaeUPO}$) of 41,700 in the anodic site, while N_2 was reduced to NH_3 at the rate of 1.38 μg h^{-1} in the cathodic site. Note that (*R*)-1-phenylethanol was not further oxidized to acetophenone (Fig. 4b), which indicates the high selectivity in enantioselective hydroxylation. The molar ratio of NH_3 to (*R*)-1-phenylethanol was estimated to be 1:16 (Fig. S22), which is different from the molar ratio (2:3) for coupling of NRR and r*Aae*UPO catalysis (N_2 + 3R-H + $3H_2O \rightarrow 2NH_3$ + 3R-OH). We attribute it to another possible oxidation-reduction coupling, such as H_2 evolution and enzymatic oxyfunctionalization (R-H + $H_2O \rightarrow$ R-OH + H_2) (Fig. S5). Furthermore, the Mo:$BiVO_4$|Si(1.80 V)/α-Fe_2O_3 platform was applied to other oxyfunctionalization reactions such as enantioselective hydroxylation of tetralin ($TOF_{rAaeUPO}$ = 9620 h^{-1}, $TTN_{rAaeUPO}$ = 57,700, e.e. > 99%) and cyclohexane ($TOF_{rAaeUPO}$ = 5600 h^{-1}, $TTN_{rAaeUPO}$ = 33,600) (Figs. 4b, S20, and S21). All of the unbiased enzymatic reactions required light, Si PV, r*Aae*UPO, and substrate (Figs. 4a and S23).

Based on the widely accepted PEC mechanism [16,25,47–50], we propose a bias-free pathway of integrating NRR with r*Aae*UPO-mediated oxygenation reactions (Fig. 4c). Both photoelectrodes (i.e., Mo:$BiVO_4$ and Si) absorb solar light to generate photoexcited electrons and holes with the corresponding quasi-Fermi levels of electrons ($E_{f,n}$) and holes ($E_{f,h}$), respectively. Because $E_{f,h}$ is more positive than the redox potential of two-electron H_2O oxidation, the Mo:$BiVO_4$ photoanode transfers its photoexcited holes to H_2O and produces H_2O_2. Subsequently, r*Aae*UPO consumes H_2O_2 and generates the catalytically active oxoferryl heme that catalyzes enantioselective oxygenation [12]. The photoexcited electrons of the Mo:$BiVO_4$ are recombined with the Si PV's photoexcited holes, whereas Si PV's photoexcited electrons are delivered to the α-Fe_2O_3's conduction band. The excited electrons then participate in N_2-to-NH_3 conversion at the surface of α-Fe_2O_3 because $E_{f,n}$ is more negative than the redox potential of six-electron reduction of N_2. In terms of voltage, Mo:$BiVO_4$ photoelectrode and Si PV harvests solar light to generate a V_{ph} (= $|E_{f,n} - E_{f,h}|$) of approximately 1.45 V (Fig. S24) and 1.80 V, respectively. The total V_{ph} (~3.25 V) is larger than the thermodynamic voltage and overpotentials for integrating N_2 fixation with H_2O oxidation, enabling the unbiased target reaction.

4. Discussion

The PEC NRR system has emerged as a promising platform to convert N_2 into NH_3, which combines the advantages of electrocatalytic and photocatalytic processes. This approach harvests clean solar energy to generate photoexcited charge carriers and applies an electrical bias to increase the redox abilities of the charge carriers. In this sense, the majority of PEC systems [9,10,51,52] have focused on developing NRR half-reaction in a three-electrode configuration, which must need an electrical potential between a working electrode and a reference electrode. In addition, the three-electrode configuration requires a counter electrode to balance the current of the working electrode, which indicates that an anodic reaction at the counter electrode is not the concern of the previous PEC NRR studies [53].

Moving beyond the conventional approach, we established the unbiased photoelectrocatalytic pairing of NRR with WOR or biocatalytic synthesis in two-electrode configuration, which converts N_2 and H_2O to value-added chemicals (e.g., NH_3, enantiopure alcohols). This simultaneous NRR and enzymatic oxygenation occurs at individual half-reaction sites. The Mo:$BiVO_4$-based photoanodes exhibit a relatively small bandgap (2.5 eV) and a positive quasi-Fermi level of holes [46], which is advantageous for solar-driven WOR. The photoactivated Si PV makes electrons' potential more negative to facilitate NRR on the α-Fe_2O_3 catalyst. We assembled these photoelectrocatalysts to construct a full PEC system that converts solar light, N_2, and H_2O to valuable compounds without external electrical bias. The PEC system compares favorably with a state-of-the-art PEC platform [24] that anodically activates r*Aae*UPO (Fig. 5). The reported PEC cell drove r*Aae*UPO catalysis ($TTN_{rAaeUPO}$ = 10,000, $TOF_{rAaeUPO}$ = 5000 h^{-1}) at 0.8 V. The $TTN_{rAaeUPO}$ and $TOF_{rAaeUPO}$ of the Mo:$BiVO_4$|Si/α-Fe_2O_3 assembly were higher even under bias-free conditions. Follow-up studies are needed to improve NH_3 production rate through, for example, (i) elucidating the detailed mechanism of O_V using computational quantum mechanical modeling methods, (ii) controlling O_V densities to increase the active site for NRR, and (iii) constructing a hydrophobic support on the α-Fe_2O_3 to suppress HER. In addition, modification of surface morphology of Mo:$BiVO_4$-based photoanodes would increase hole concentrations at the photoanode|electrolyte interface [54], which accelerates the photoanodic performance of electron extraction from H_2O. These studies will broaden the scope of the platform to other redox reactions (e.g., lignin valorization, alcohol oxidation, enzymatic dehydrogenation) [41,55] with enhanced productivities.

5. Conclusion

We report bias-free pairing of NRR with WOR and UPO biocatalysis in a two-electrode configuration using Si/α-Fe_2O_3 photocathode and Mo:$BiVO_4$-based photoanode. The photocathodic half-reaction occurred via (i) transfer of photoexcited electrons from Si to α-Fe_2O_3 and (ii) electrocatalytic reduction of N_2 to NH_3 at the surface of α-Fe_2O_3. To

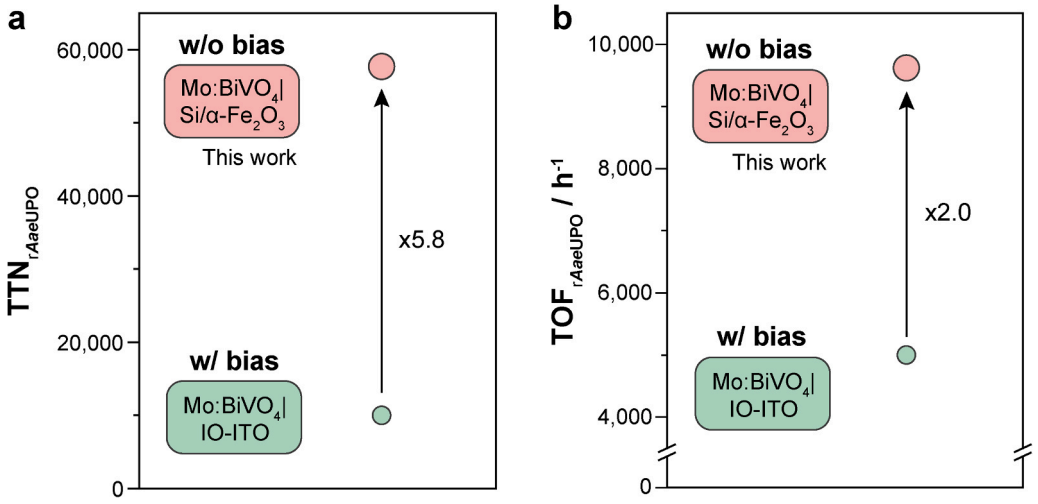

Fig. 5. Comparison of r*Aae*UPO-hybrid PEC systems for anodic oxyfunctionalization reactions in terms of (**a**) $TTN_{rAaeUPO}$ and (**b**) $TOF_{rAaeUPO}$ values. Assembly: Mo:$BiVO_4$|IO-ITO (green; ref. [24]). IO-ITO, inverse opal-structured indium tin oxide.

accelerate NH_3 production, we synthesized the α-Fe_2O_3 under O_2-depleted environments, which increased (i) the number ratio of O_V by 1.33 times and (ii) the rate of NH_3 production by 1.37 times. Concurrently, the photoanodic half-reaction by Mo:$BiVO_4$-based energy materials led to the extraction of electrons from H_2O and the transfer of them to the photocathode. To boost the photoanodic H_2O oxidation, we deposited the FeOOH adlayer on the Mo:$BiVO_4$ photoanode, which gave rise to an increase in charge separation efficiencies ($\eta_{surface}$ of 22–53%), a decrease in charge-transfer resistance by up to 1.44 times, a decrease in Tafel slope by 1.3 times, and a suppression of charge recombination. In addition, NH_3 production rate increased with increasing H_2O concentration, which highlighted the role of H_2O as an electron donor for N_2 reduction. When we combined PEC NRR with r*Aae*UPO-catalyzed oxyfunctionalization reactions, we used Mo:$BiVO_4$ photoanode that (i) receives holes from NRR reaction, (ii) oxidizes H_2O to H_2O_2, and (iii) generates r*Aae*UPO's the catalytically active oxoferryl heme. Overall, the unbiased NRR platform produced valuable compounds at the photoanodic and photocathodic compartments through enantioselective hydroxylation as well as N_2 reduction.

CRediT authorship contribution statement

Chang Hyun Kim: Conceptualization, Formal analysis, Investigation, Methodology, Visualization, Validation, Writing - original draft, Writing - review & editing. **Jinhyun Kim:** Conceptualization, Formal analysis, Investigation, Methodology, Visualization, Supervision, Validation, Writing - original draft, Writing - review & editing. **Frank Hollmann:** Resources. **Chan Beum Park:** Resources, Supervision, Funding acquisition, Project administration, Writing - original draft, Writing - review & editing.

Declaration of Competing Interest

The authors declare that they have no known competing financial interests or personal relationships that could have appeared to influence the work reported in this paper.

Data availability

Data will be made available on request.

Acknowledgments

This work was supported by the National Research Foundation (NRF) via the Creative Research Initiative Center (grant no. NRF-2015R1A3A2066191), Republic of Korea. We thank Professor Byungha Shin and Dr. Choongman Moon at KAIST for quantifying gas molecules.

Appendix A. Supporting information

Supplementary data associated with this article can be found in the online version at doi:10.1016/j.apcatb.2023.122925.

References

[1] G. Qing, R. Ghazfar, S.T. Jackowski, F. Habibzadeh, M.M. Ashtiani, C.-P. Chen, M. R. Smith, T.W. Hamann, Recent advances and challenges of electrocatalytic N_2 reduction to ammonia, Chem. Rev. 120 (2020) 5437–5516.
[2] B.H.R. Suryanto, K. Matuszek, J. Choi, R.Y. Hodgetts, H.-L. Du, J.M. Bakker, C.S. M. Kang, P.V. Cherepanov, A.N. Simonov, D.R. MacFarlane, Nitrogen reduction to ammonia at high efficiency and rates based on a phosphonium proton shuttle, Science 372 (2021) 1187–1191.
[3] J.G. Chen, R.M. Crooks, L.C. Seefeldt, K.L. Bren, R.M. Bullock, M.Y. Darensbourg, P.L. Holland, B. Hoffman, M.J. Janik, A.K. Jones, M.G. Kanatzidis, P. King, K. M. Lancaster, S.V. Lymar, P. Pfromm, W.F. Schneider, R.R. Schrock, Beyond fossil fuel-driven nitrogen transformations, Science 360 (2018), eaar6611.
[4] B.H.R. Suryanto, H.-L. Du, D. Wang, J. Chen, A.N. Simonov, D.R. MacFarlane, Challenges and prospects in the catalysis of electroreduction of nitrogen to ammonia, Nat. Catal. 2 (2019) 290–296.
[5] Y. Pang, C. Su, G. Jia, L. Xu, Z. Shao, Emerging two-dimensional nanomaterials for electrochemical nitrogen reduction, Chem. Soc. Rev. 50 (2021) 12744–12787.
[6] Y. Liu, J. Lu, Q. Zhang, Y. Bai, X. Pang, S. Wang, H. Bai, W. Fan, Charge-transfer dynamics at a Ag/Ni-MOF/Cu_2O heterostructure in photoelectrochemical NH_3 production, Chem. Commun. 57 (2021) 8031–8034.
[7] S. Shang, W. Xiong, C. Yang, B. Johannessen, R. Liu, H.-Y. Hsu, Q. Gu, M.K. H. Leung, J. Shang, Atomically dispersed iron metal site in a porphyrin-based metal–organic framework for photocatalytic nitrogen fixation, ACS Nano 15 (2021) 9670–9678.
[8] A. Banerjee, B.D. Yuhas, E.A. Margulies, Y. Zhang, Y. Shim, M.R. Wasielewski, M. G. Kanatzidis, Photochemical nitrogen conversion to ammonia in ambient conditions with FeMoS-chalcogels, J. Am. Chem. Soc. 137 (2015) 2030–2034.
[9] Y. Bai, H. Bai, Z. Fang, X. Li, W. Fan, W. Shi, Understanding the Z-scheme heterojunction of $BiVO_4$/PANI for photoelectrochemical nitrogen reduction, Chem. Commun. 57 (2021) 10568–10571.
[10] M. Li, Q. Lu, M. Liu, P. Yin, C. Wu, H. Li, Y. Zhang, S. Yao, Photoinduced charge separation via the double-electron transfer mechanism in nitrogen vacancies g-C_3N_5/BiOBr for the photoelectrochemical nitrogen reduction, ACS Appl. Mater. Interfaces 12 (2020) 38266–38274.
[11] J. Kim, S.H. Lee, F. Tieves, C.E. Paul, F. Hollmann, C.B. Park, Nicotinamide adenine dinucleotide as a photocatalyst, Sci. Adv. 5 (2019), eaax0501.
[12] J. Kim, T.V.T. Nguyen, Y.H. Kim, F. Hollmann, C.B. Park, Lignin as a multifunctional photocatalyst for solar-powered biocatalytic oxyfunctionalization of C–H bonds, Nat. Synth. 1 (2022) 217–226.
[13] J. Kim, J. Jang, T. Hilberath, F. Hollmann, C.B. Park, Photoelectrocatalytic biosynthesis fuelled by microplastics, Nat. Synth. 1 (2022) 776–786.
[14] J. Yoon, H. Jang, M.-W. Oh, T. Hilberath, F. Hollmann, Y.S. Jung, C.B. Park, Heat-fueled enzymatic cascade for selective oxyfunctionalization of hydrocarbons, Nat. Commun. 13 (2022) 3741.
[15] J. Yoon, J. Kim, F. Tieves, W. Zhang, M. Alcalde, F. Hollmann, C.B. Park, Piezobiocatalysis: ultrasound-driven enzymatic oxyfunctionalization of C–H bonds, ACS Catal. 10 (2020) 5236–5242.
[16] J. Kim, Y. Um, S. Han, T. Hilberath, Y.H. Kim, F. Hollmann, C.B. Park, Unbiased photoelectrode interfaces for solar coupling of lignin oxidation with biocatalytic C=C bond hydrogenation, ACS Appl. Mater. Interfaces 14 (2022) 11465–11473.
[17] S. Liu, T. Qian, M. Wang, H. Ji, X. Shen, C. Wang, C. Yan, Proton-filtering covalent organic frameworks with superior nitrogen penetration flux promote ambient ammonia synthesis, Nat. Catal. 4 (2021) 322–331.
[18] M.I. Ahmed, C. Liu, Y. Zhao, W. Ren, X. Chen, S. Chen, C. Zhao, Metal–sulfur linkages achieved by organic tethering of ruthenium nanocrystals for enhanced electrochemical nitrogen reduction, Angew. Chem. Int. Ed. 59 (2020) 21465–21469.
[19] Z. Sun, R. Huo, C. Choi, S. Hong, T.-S. Wu, J. Qiu, C. Yan, Z. Han, Y. Liu, Y.-L. Soo, Y. Jung, Oxygen vacancy enables electrochemical N_2 fixation over WO_3 with tailored structure, Nano Energy 62 (2019) 869–875.
[20] Z. Han, C. Choi, S. Hong, T.-S. Wu, Y.-L. Soo, Y. Jung, J. Qiu, Z. Sun, Activated TiO_2 with tuned vacancy for efficient electrochemical nitrogen reduction, Appl. Catal. B Environ. 257 (2019), 117896.
[21] Y. Zhao, Y. Zhao, R. Shi, B. Wang, G.I.N. Waterhouse, L.-Z. Wu, C.-H. Tung, T. Zhang, Tuning oxygen vacancies in ultrathin TiO_2 nanosheets to boost photocatalytic nitrogen fixation up to 700 nm, Adv. Mater. 31 (2019), 1806482.
[22] K. Chu, F. Liu, J. Zhu, H. Fu, H. Zhu, Y. Zhu, Y. Zhang, F. Lai, T. Liu, A general strategy to boost electrocatalytic nitrogen reduction on perovskite oxides via the oxygen vacancies derived from A-site deficiency, Adv. Energy Mater. 11 (2021), 2003799.
[23] Z. Wang, X. Mao, P. Chen, M. Xiao, S.A. Monny, S. Wang, M. Konarova, A. Du, L. Wang, Understanding the roles of oxygen vacancies in hematite-based photoelectrochemical processes, Angew. Chem. Int. Ed. 58 (2019) 1030–1034.
[24] D.S. Choi, J. Kim, F. Hollmann, C.B. Park, Solar-assisted ebiorefinery: photoelectrochemical pairing of oxyfunctionalization and hydrogenation reactions, Angew. Chem. Int. Ed. 59 (2020) 15886–15890.
[25] J. Kim, Y.W. Lee, E.-G. Choi, P. Boonmongkolras, B.W. Jeon, H. Lee, S.T. Kim, S. K. Kuk, Y.H. Kim, B. Shin, C.B. Park, Robust FeOOH/$BiVO_4$/Cu(In, Ga)Se_2 tandem structure for solar-powered biocatalytic CO_2 reduction, J. Mater. Chem. A 8 (2020) 8496–8502.
[26] K. Kim, C.B. Park, Femtomolar sensing of Alzheimer's tau proteins by water oxidation-coupled photoelectrochemical platform, Biosens. Bioelectron. 154 (2020), 112075.
[27] K.J. McDonald, K.-S. Choi, A new electrochemical synthesis route for a BiOI electrode and its conversion to a highly efficient porous $BiVO_4$ photoanode for solar water oxidation, Energy Environ. Sci. 5 (2012) 8553–8557.
[28] B. Zhang, L. Wang, Y. Zhang, Y. Ding, Y. Bi, Ultrathin FeOOH nanolayers with abundant oxygen vacancies on $BiVO_4$ photoanodes for efficient water oxidation, Angew. Chem. Int. Ed. 57 (2018) 2248–2252.
[29] X. Li, W. Fan, Y. Bai, Y. Liu, F. Wang, H. Bai, W. Shi, Photoelectrochemical reduction of nitrate to ammonia over CuPc/CeO_2 heterostructure: understanding the synergistic effect between oxygen vacancies and Ce sites, Chem. Eng. J. 433 (2022), 133225.
[30] F. Wang, Q. Ding, J. Ding, Y. Bai, H. Bai, W. Fan, Frustrated Lewis pairs boosting photoelectrochemical nitrate reduction over $ZnIn_2S_4$/$BiVO_4$ heterostructure, Chem. Eng. J. 450 (2022), 138260.
[31] J. Kim, S.H. Lee, F. Tieves, D.S. Choi, F. Hollmann, C.E. Paul, C.B. Park, Biocatalytic C=C bond reduction through carbon nanodot-sensitized regeneration of NADH analogues, Angew. Chem. Int. Ed. 57 (2018) 13825–13828.
[32] D. Wang, S.H. Lee, S. Han, J. Kim, N.V.T. Trang, K. Kim, E.-G. Choi, P. Boonmongkolras, Y.W. Lee, B. Shin, Y.H. Kim, C.B. Park, Lignin-fueled

photoelectrochemical platform for light-driven redox biotransformation, Green Chem. 22 (2020) 5151–5160.
[33] G. Son, J. Kim, C.B. Park, Interference of solvatochromic twist in amyloid nanostructure for light-driven biocatalysis, ACS Appl. Energy Mater. 3 (2020) 1215–1221.
[34] T.-K. Le, J. Kim, N.A. Nguyen, T.H.H. Nguyen, E.-G. Sun, S.-M. Yee, H.-S. Kang, S.-J. Yeom, C.B. Park, C.-H. Yun, Solar-powered whole-cell P450 catalytic platform for C-hydroxylation reactions, ChemSusChem 14 (2021) 3054–3058.
[35] D. Wang, J. Kim, C.B. Park, Lignin-induced $CaCO_3$ vaterite structure for biocatalytic artificial photosynthesis, ACS Appl. Mater. Interfaces 13 (2021) 58522–58531.
[36] M. Hobisch, M.M.C.H. van Schie, J. Kim, K. Røjkjær Andersen, M. Alcalde, R. Kourist, C.B. Park, F. Hollmann, S. Kara, Solvent-free photobiocatalytic hydroxylation of cyclohexane, ChemCatChem 12 (2020) 4009–4013.
[37] Y.W. Lee, P. Boonmongkolras, E.J. Son, J. Kim, S.H. Lee, S.K. Kuk, J.W. Ko, B. Shin, C.B. Park, Unbiased biocatalytic solar-to-chemical conversion by FeOOH/$BiVO_4$/perovskite tandem structure, Nat. Commun. 9 (2018) 4208.
[38] Y. Zhang, Z. Xiong, Y. Li, M. Wilson, K.E. Christensen, E. Jaques, P. Hernández-Lladó, J. Robertson, L.L. Wong, Enantioselective oxidation of unactivated C–H bonds in cyclic amines by iterative docking-guided mutagenesis of P450BM3 (CYP102A1), Nat. Synth. 1 (2022) 936–945.
[39] D.C. Miller, S.V. Athavale, F.H. Arnold, Combining chemistry and protein engineering for new-to-nature biocatalysis, Nat. Synth. 1 (2022) 18–23.
[40] M.A. Herrera, D.J. Campopiano, Buy one, get one free, Nat. Synth. 1 (2022) 420–421.
[41] C.-H. Yun, J. Kim, F. Hollmann, C.B. Park, Light-driven biocatalytic oxidation, Chem. Sci. 13 (2022) 12260–12279.
[42] H.S. Soo, Solar-powered biorefinery, Nat. Synth. 1 (2022) 192–193.
[43] D.G. Boucher, S.D. Minteer, Making molecules with microplastics, Nat. Synth. 1 (2022) 751–752.
[44] F. Tieves, S.J.-P. Willot, M.M.C.H. vanSchie, M.C.R. Rauch, S.H.H. Younes, W. Zhang, J. Dong, P. GomezdeSantos, J.M. Robbins, B. Bommarius, M. Alcalde, A. S. Bommarius, F. Hollmann, Formate oxidase (FOx) from aspergillus oryzae: one catalyst enables diverse H_2O_2-dependent biocatalytic oxidation reactions, Angew. Chem. Int. Ed. 58 (2019) 7873–7877.
[45] W. Zhang, H. Liu, M.M.C.H. van Schie, P.-L. Hagedoorn, M. Alcalde, A.G. Denkova, K. Djanashvili, F. Hollmann, Nuclear waste and biocatalysis: a sustainable liaison? ACS Catal. 10 (2020) 14195–14200.
[46] J.H. Kim, J.S. Lee, Elaborately modified $BiVO_4$ photoanodes for solar water splitting, Adv. Mater. 31 (2019), 1806938.
[47] S.K. Kuk, J. Jang, J. Kim, Y. Lee, Y.S. Kim, B. Koo, Y.W. Lee, J.W. Ko, B. Shin, J.-K. Lee, C.B. Park, CO_2-reductive, copper oxide-based photobiocathode for Z-scheme semi-artificial leaf structure, ChemSusChem 13 (2020) 2940–2944.
[48] J. Kim, C.B. Park, Shedding light on biocatalysis: photoelectrochemical platforms for solar-driven biotransformation, Curr. Opin. Chem. Biol. 49 (2019) 122–129.
[49] J. Kim, C.B. Park, Artificial photosynthetic biohybrids for CO_2 and N_2 fixation, Chem. Catal. 2 (2022) 2425–2427.
[50] C.H. Lee, J. Kim, C.B. Park, Z-schematic artificial leaf structure for biosolar oxyfunctionalization of hydrocarbons, ACS Energy Lett. 8 (2023) 2513–2521.
[51] Y. Bai, H. Bai, K. Qu, F. Wang, P. Guan, D. Xu, W. Fan, W. Shi, In-situ approach to fabricate BiOI photocathode with oxygen vacancies: understanding the N_2 reduced behavior in photoelectrochemical system, Chem. Eng. J. 362 (2019) 349–356.
[52] M.S. Yu, S.C. Jesudass, S. Surendran, J.Y. Kim, U. Sim, M.-K. Han, Synergistic interaction of MoS_2 nanoflakes on $La_2Zr_2O_7$ nanofibers for improving photoelectrochemical nitrogen reduction, ACS Appl. Mater. Interfaces 14 (2022) 31889–31899.
[53] A.J. Bard, L.R. Faulkner, Electrochemical Methods: Fundamentals and Applications, Wiley, 2000.
[54] H. Bai, F. Wang, Q. Ding, W. Xie, H. Li, G. Zheng, W. Fan, Construction of frustrated Lewis pair sites in CeO_2–C/$BiVO_4$ for photoelectrochemical nitrate reduction, Inorg. Chem. 62 (2023) 2394–2403.
[55] J. Kim, C.B. Park, Collaborative catalysis for solar biosynthesis, Trends Chem. 5 (2023) 133–146.